

Check for updates

Self-Timed and Spatially Targeted Delivery of Chemical Cargo by Motile Liquid Crystal

Xin Wang, Yu Yang, Sangchul Roh, Sarah Hormozi, Nathan C. Gianneschi, and Nicholas L. Abbott*

A key challenge underlying the design of miniature machines is encoding materials with time- and space-specific functional behaviors that require little human intervention. Dissipative processes that drive materials beyond equilibrium and evolve continuously with time and location represent one promising strategy to achieve such complex functions. This work reports how internal nonequilibrium states of liquid crystal (LC) emulsion droplets undergoing chemotaxis can be used to time the delivery of a chemical agent to a targeted location. During ballistic motion, hydrodynamic shear forces dominate LC elastic interactions, dispersing microdroplet inclusions (microcargo) within double emulsion droplets. Scale-dependent colloidal forces then hinder the escape of dispersed microcargo from the propelling droplet. Upon arrival at the targeted location, a circulatory flow of diminished strength allows the microcargo to cluster within the LC elastic environment such that hydrodynamic forces grow to exceed colloidal forces and thus trigger the escape of the microcargo. This work illustrates the utility of the approach by using microcargo that initiate polymerization upon release through the outer interface of the carrier droplet. These findings provide a platform that utilizes nonequilibrium strategies to design autonomous spatial and temporal functions into active materials.

1. Introduction

Biological systems make extensive use of active processes^[1] in which chemical fuels (e.g., adenosine triphosphate, ATP) are used to drive dissipative processes, such as during cellular

X. Wang, Y. Yang, S. Roh, S. Hormozi, N. L. Abbott Smith School of Chemical and Biomolecular Engineering Cornell University

Ithaca, NY 14850, USA E-mail: nla34@cornell.edu

S. Roh

School of Chemical Engineering Chonnam National University Gwangju 61186, Republic of Korea

N. C. Gianneschi Department of Chemistry, Materials Science & Engineering, Biomedical Engineering and Pharmacology Northwestern University Evanston, IL 60208, USA

The ORCID identification number(s) for the author(s) of this article can be found under https://doi.org/10.1002/adma.202311311

DOI: 10.1002/adma.202311311

motility^[2,3] (e.g., leukocyte migration)^[4,5] or embryonic development.^[6] During these active processes, chemical signals often polarize the direction of motion (chemotaxis) to spatially target a desired outcome. [4,6] Additionally, the timing of sequential events, such as gastrulation during development of fly embryo, involves triggering via dissipative flows within the cells.^[7] Inspired by these strategies, here we explore the design of synthetic soft matter systems that seek to recapitulate key aspects of such behaviors. In particular, we sought to determine if it is possible to exploit dissipative processes internal to self-propelling liquid crystal (LC) double emulsion droplets to time the delivery and release of a functional chemical species at a targeted location (Figure 1). We illustrate the approach by delivery of an initiator for polymerization.

To achieve self-propelled motion of a double emulsion LC droplet, the droplet must have the ability to convert (chemical potential) energy in the system into mechanical work (i.e., function as active matter).^[8–12] We use the Marangoni effect, an interfacial

flow driven by a spatial gradient in interfacial energy that has been shown previously to be sustained by solubilization of oil at the interface of an oil droplet immersed in a micellar solution of surfactant.[11-17] Because the Marangoni effect generates advective flows both inside and outside of the oil droplet, [18,19] in this manuscript, we show that Marangoni flows can also be used to drive internal dissipative processes within double emulsion LC droplets to time the release and thus delivery of microcargo (i.e., surfactant-stabilized aqueous inclusions that contain reactive species) to a targeted location. We show that dissipative processes internal to the LC double emulsion control the microcargo cluster sizes and thus hydrodynamic forces that compete with repulsive colloidal forces at the carrier droplet interface to time the release of microcargo at the desired location. This strategy contrasts to past studies in which collisions of active droplets with an object^[20] or spatially localized stimuli (e.g., light or pH) have been used to trigger release.^[21,22] We illustrate our approach by delivering an initiator for polymerization, but the principles are applicable to a range of functional ingredients that can be hosted in the microcargo (e.g., drugs, dyes, antibacterial agents, and/or nutrients).

15214095, 2024, 28, Downloaded from https://onlinelbray.wiley.com/doi/10.1002/adma.20211311 by Cornell University Library. Wiley Online Library on [2208/2024]. See the Terms and Conditions (https://onlinelibray.wiley.com/terms-and-conditions) on Wiley Online Library for rules of use; OA articles are governed by the applicable Creative Commons Licenses

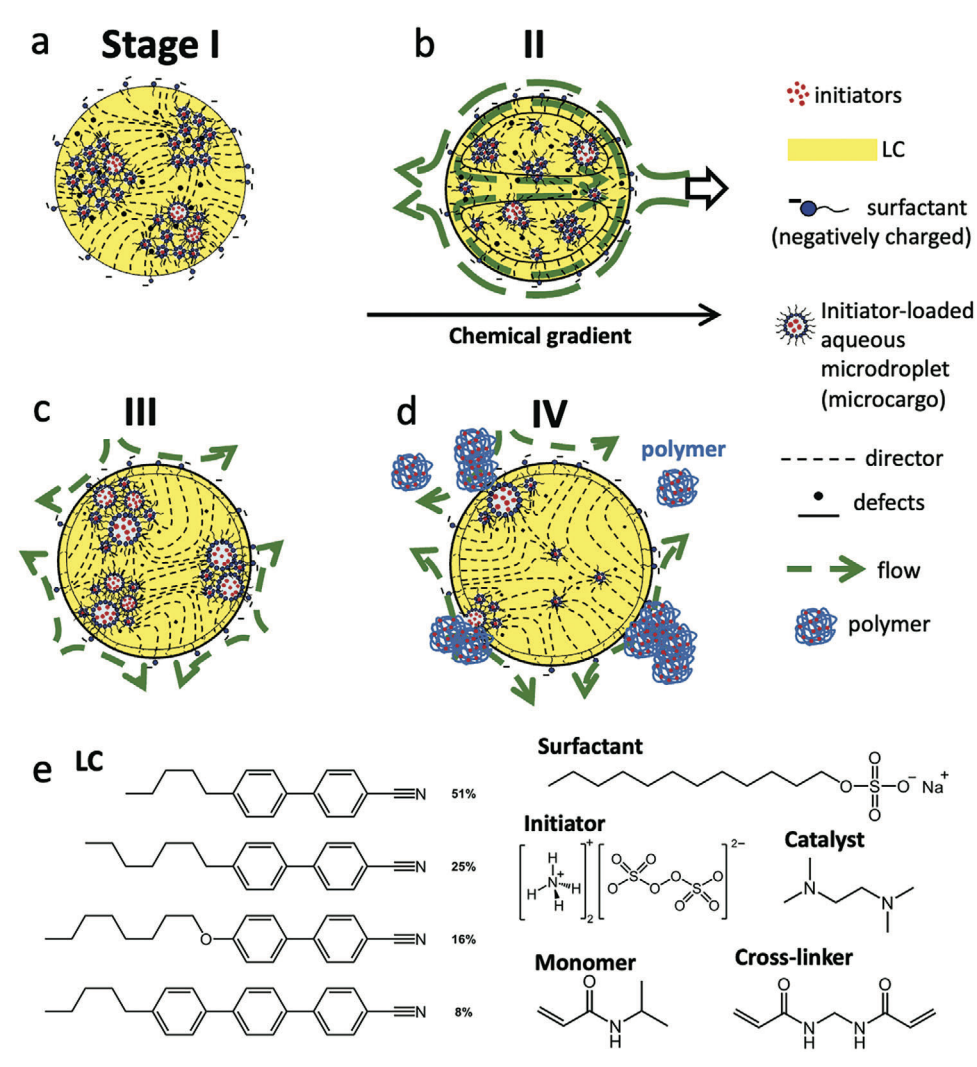


Figure 1. Design of chemotactic self-timed delivery system and molecular constituents. a—d) Schematic illustrations of the system. The liquid crystal (LC) carrier droplet is a double emulsion. a) An initiator of polymerization is loaded into the interior aqueous microdroplets (microcargo) that are stabilized by a surfactant within the LC oil (red dots). b) The LC carrier droplet can self-propel and move to a targeted location with a chemical gradient dictating its directional ballistic motion. c) Once the LC carrier droplet arrives at its destination, a combination of advection internal to the LC carrier droplet and LC elasticity leads to coarsening and clustering of the microcargo and d) autonomous release of microcargo into the aqueous phase surrounding the LC droplet. Polymerization is subsequently triggered in the outer monomer solution. e) Molecular structures of E7 (LC), sodium dodecyl sulfate (SDS, surfactant), ammonium persulfate (APS, initiator), N,N,N',N'-tetramethylethylenediamine (TEMED, catalyst), N-isopropylacrylamide (NIPAm, monomer) and N,N'-methylenebis(acrylamide) (BIS, cross-linker).

2. Results and Discussion

2.1. Macroscopic Observations

We prepared millimeter-sized water-in-LC-in-water double emulsions (Figure 1, Experimental Section), which we term LC carrier droplets in the remainder of this paper. The aqueous microdroplets within the LC carrier droplets (microcargo) were stabilized by an anionic surfactant (sodium dodecyl sulfate, SDS) and hosted a chemical initiator for free radical polymerization (ammonium persulfate, APS). We used a nematic LC (E7, Figure 1e) as the oil to form the double emulsion because the LC elastically traps microcargo inside the LC carrier droplets (Figure 1a). [23,24] In addition, the LC elasticity mediates long-range (100 µm) and short-range (1 µm) interactions between microcargo which, as

described below, play a central role in timing the release of the microcargo. We used concentration gradients of surfactant and monomer in aqueous solution to drive the motion of the carrier droplets (chemotaxis, [15,25,26] Figure 1b). We generated the gradients by contacting two solutions with distinct compositions (see below). In initial experiments, we added dye to observe the chemical gradients (Figure S1, Supporting Information, shows the time-dependent chemical gradient), which revealed that reproducible gradients are generated from a combination of convective and diffusive transport processes (see Supporting Information).

When imaging LC carrier droplets in the sample chamber, each droplet was observed to be opaque against a black background because light was scattered by the LC and aqueous microcargo inside the carrier droplets (Figure 2). Macroscopically,

15214095, 2024, 28, Downloaded from https://onlinelibrary.wiley.com/doi/10.1002/adma.202311311 by Cornell University Library. Wiley Online Library on [22.08/2024]. See the Terms and Conditions (https://onlinelibrary.wiley.com/terms-and-

conditions) on Wiley Online Library for rules of use; OA articles are governed by the applicable Creative Commons I

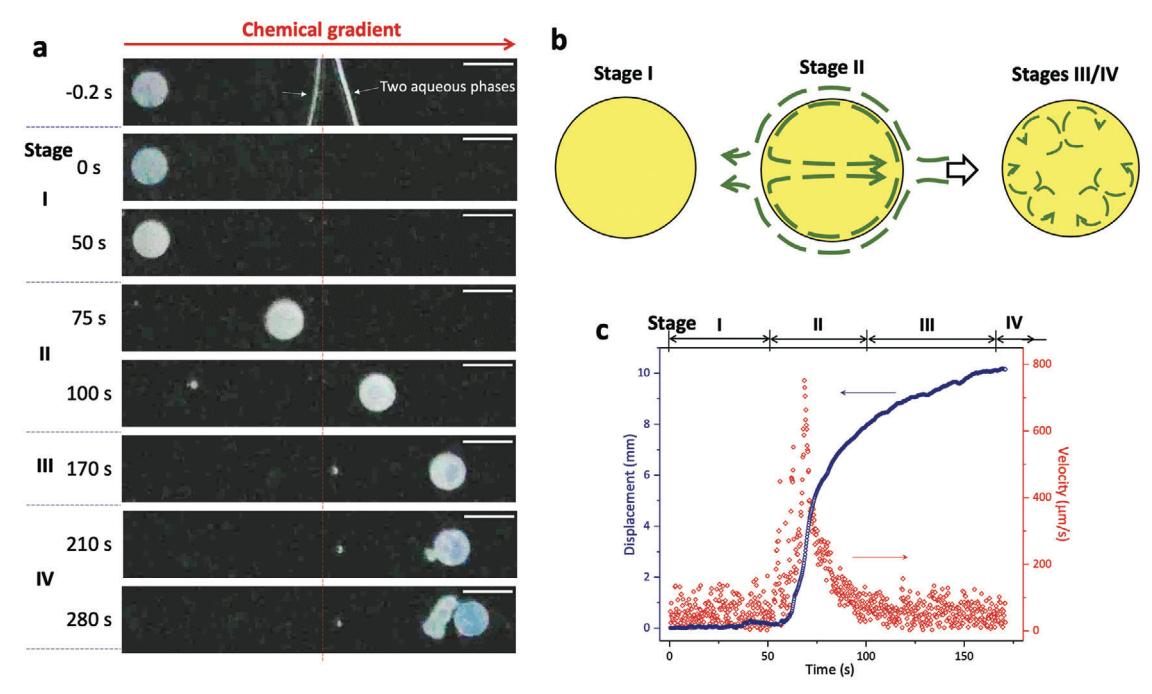


Figure 2. Chemotactic liquid crystal (LC) carrier droplet self-propels along a chemical gradient and autonomously releases microcargo at a targeted location to trigger polymerization. a) Images of a LC carrier droplet as a function of time. Stage I: The first image (-0.2 s) shows the two aqueous phases, a carrier droplet in 5×10^{-3} M SDS solution (left) and a surfactant/monomer solution (right, 1 M SDS, 20 wt% monomers, monomer: cross-linker = 100:1, 1 vol% catalyst, 35 °C), before contact. The surfaces of the two phases appear as bright lines in the image (indicated by white arrows). Stage II: Ballistic movement of the LC carrier droplet toward the region of high chemical concentration was observed (50-110 s). Stage III: The LC carrier droplet exhibited slow center of mass displacement with coarsening and reorganization of microdroplet inclusions (microcargo) (110-170 s). Stage IV: The LC carrier droplet released the microcargo containing initiator and triggered polymerization of the monomer (170-280 s). The appearance of the carrier droplet changed from opaque to relatively transparent as microcargo were released. Scale bars, 2 mm. b) Schematic illustrations of flow fields within LC carrier droplets at different stages of the LC carrier droplet behavior. Green arrows indicate fluid flow. White arrow denotes droplet motion. c) Displacement and velocity of the LC carrier droplet as a function of time.

we found that the LC carrier droplets in the sample chamber could be categorized as exhibiting four stages of dynamic behavior (Figures 1 and 2, Video S1, Supporting Information). Stage I, Initial Stationary State: prior to arrival of the chemical gradient at the location of the LC carrier droplet (Figure 2a,b, -0.2 to 50 s), the droplet was stationary as it was too large to exhibit measurable Brownian motion. The microcargo were clustered but immobile and trapped within the carrier droplet (Figure 1a). We observed the droplet to exhibit motion approximately 50 s after contact of the two solutions (Figure 2a, 50 s), which coincided with the arrival of the chemical gradient at the location of the LC carrier droplet (Figure S1, Supporting Information). Stage II, Directional Motion: the LC carrier droplet moved ballistically toward the region of high surfactant and monomer concentration, consistent with the predicted effects of Marangoni flows generated at the interface of the droplet. Within the carrier droplet, a single axisymmetric circulating flow (Figure 2b, Figure S2, Supporting Information)[17,18] caused microcargo to circulate but the microcargo remained trapped within the carrier droplet (Figure 1b). The self-propelled ballistic motion of the carrier droplet persisted for almost a minute (50-110s) with the velocity of the droplet rapidly increasing to 800 µms⁻¹ and then decreasing to 50–0 µms⁻¹ (Figure 2c). The droplet in Figure 2 moved approximately 10 mm during Stage II.

The next two stages of behavior, Stage III: Reorganization (Figure 2a, 110-170 s) and Stage IV: Release (Figure 2a, 170-280 s), were observed after the translational motion of the LC carrier droplet had largely ceased. While center of mass motion of the LC carrier droplet was minimal, advection within the LC carrier droplet persisted during both Stages III and IV, with multiple circulating flows evident near the carrier droplet interface (Figure 2b, Figure S2, Supporting Information). During Stage III, which is elucidated in microscopic detail in the next section, we observed the aqueous microcargo to coalesce and cluster under the influence of the flow internal to the LC carrier droplet (Figure 1c) but still, the microcargo was not released from the carrier droplet. In contrast, Stage IV is defined by the onset of release of the microcargo from the LC carrier droplets (Figure 1d), and subsequent triggering of polymerization in the solution surrounding the droplets (Figure 2a, 170-280 s). We performed experiments with Rose Bengal dye dissolved in the microcargo to provide an estimate of the extent of release. In experiments performed with LC carrier droplets that initially contained 10 vol% of microcargo, we measured the volume ratio of microcargo to LC after release to be 3.3 ± 0.8 vol% (n = 3). This leads us to estimate that $67 \pm 8\%$ microcargo was released. After triggering the formation of cross-linked polymer, the LC carrier droplet exhibited a transparent appearance, consistent with a decrease in the number of microcargo within the droplet (Video S2, Supporting

1521495, 2024, 28, Downoladed from https://onlinelbray.aviley.com/doi/10.1002/adma.20211111 by Cornell University Library, Wiley Online Library on [22082024], See the Terms and Conditions (https://onlinelibray.aviley.com/terms-and-conditions) on Wiley Online Library for rules of use; OA articles are governed by the applicable Creative Commons Licenses

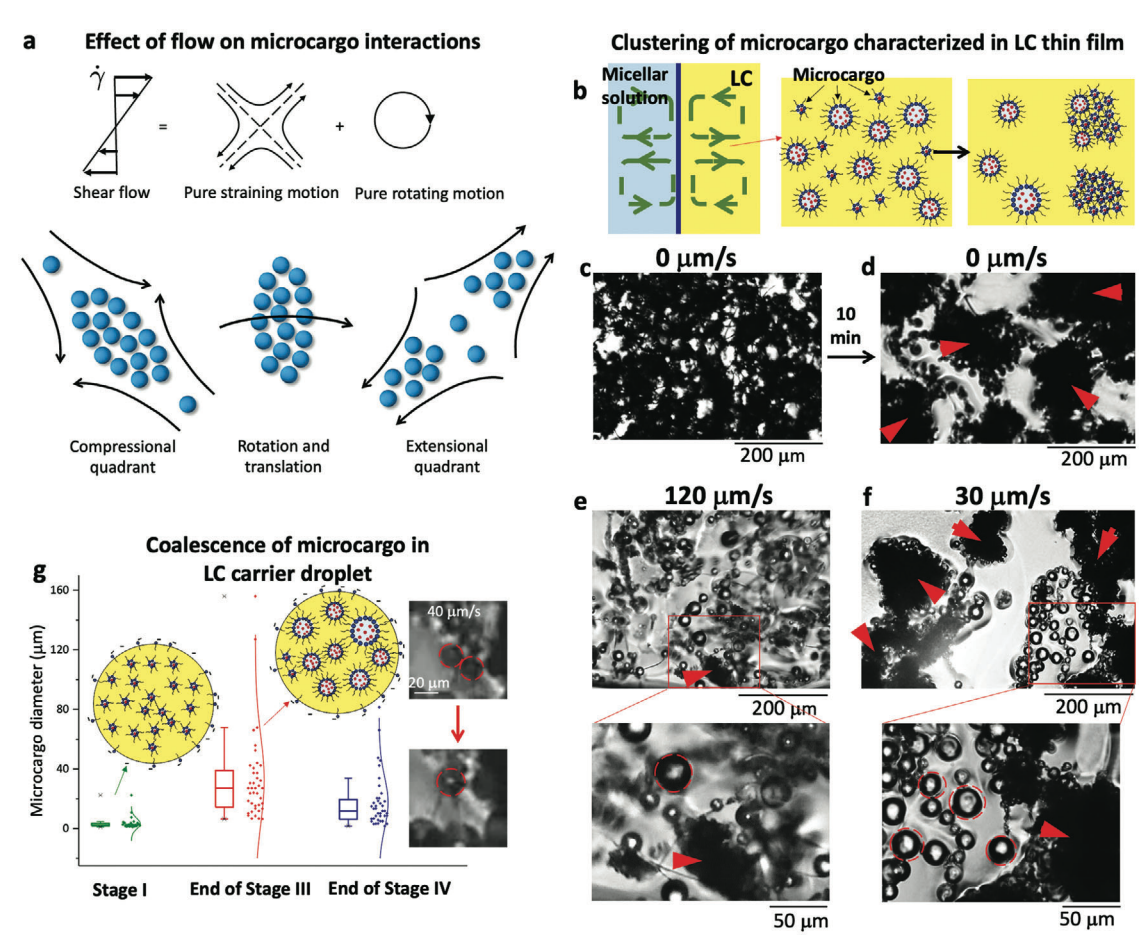


Figure 3. Stages I–III: Clustering and coalescence of microcargo inside liquid crystal (LC) films and carrier droplets with and without interfacial flows. a) Schematic illustration of the influence of flow on clustering of microcargo. b) Schematic illustrations of thin film experimental geometry (left), showing microcargo clustering over time inside the LC (middle and right). c,d) Micrographs of microcargo in the absence of flow. The formation of large clusters (denoted by red arrows) with diameters of 200–500 μ m (due to LC elasticity) is evident. e,f) Micrographs showing the influence of interfacially driven flow on microcargo organization in LC. e) A strong interfacial flow disrupts clusters more effectively than f) a weak flow (we note release occurs under both conditions). Additionally, large microcargo (10–30 μ m, in red circles) in f) favor a dispersed state as compared to small microcargo (1–5 μ m, on the right of the image). g) Change in size of microcargo in LC carrier droplets, arising from coalescence driven by circulating flows within the droplets ($n \ge 5$).

Information). All internal motion of the LC carrier droplet ceased after the release of the microcargo (\approx 10 min).

2.2. Microscopic Observations

To understand why microcargo were not released during Stages I–III, we performed microscopic observations of the dynamic behaviors of the microcargo. Our interpretation of these observations was informed by prior work showing that, at rest, LC elasticity can mediate a combination of long-range attractions^[27] between inclusions, which result in clustering, in addition to short-range repulsive interactions that typically prevent (or inhibit) coalescence.^[23,28] In addition, prior studies have shown that a shear flow can be decomposed into a straining motion and a rotating motion (**Figure 3a**). Therefore, in the compressional quadrant of a straining flow, inclusions can be transported toward each other, leading to clustering and potential coalescence (if droplets). The clusters so-formed can rotate in the shear

flow and transmit momentum over extended distances. In contrast, in the extensional quadrant, a straining flow can promote the break-up of clusters. These ideas have been explored previously in different areas of soft matter, e.g., strain thickening of hard spheres in a viscous liquid,^[29–31] force chains in granular media,^[32] friction-induced shear thickening behavior in non-Brownian suspensions,^[33] and hydroclustering in shear thickening of Brownian suspensions.^[34] Below we describe how the interplay of elasticity and flow underlies the microscopic behaviors of the microcargo in the LC carrier droplets.

Because the high density of microcargo in LC carrier droplets made imaging of cluster sizes challenging, we performed microscopic observations by preparing a thin film of LC (thickness $\approx\!100~\mu\text{m}$) containing microcargo between two microscope slides and then contacting the LC with an aqueous surfactant/monomer solution (0.8 $\,\mathrm{M}$ SDS and 5 wt% monomer). The flow fields observed within the thin films exhibited qualitative similarities to those observed in droplets during Stages I, III, and IV. Specifically, in the absence of a micellar solution (similar

15214095, 2024, 28, Downloaded from https://onlinelbray.wiley.com/doi/10.1002/adma.20211311 by Cornell University Library. Wiley Online Library on [2208/2024]. See the Terms and Conditions (https://onlinelibray.wiley.com/terms-and-conditions) on Wiley Online Library for rules of use; OA articles are governed by the applicable Creative Commons Licenses

to Stage I), there was no circulatory flow, whereas in the presence of a micellar solution (similar to Stages III and IV), multiple circulatory flows were observed near the LC-aqueous interface (Figure 3b and Figure S3, Supporting Information). However, some differences were observed between the LC droplet and film geometries. For example, the flow velocities in the thin LC films (<200 µms⁻¹) were lower than those observed in droplets, with local vortex sizes ranging from 10 to 100 µm, and the highest flow velocities occurring near the interface. The LC films also did not exhibit system-size circulations as observed during Stage II motion of droplets. Additionally, unlike the droplet experiments, the film geometry experiments began with pre-existing microcargo clusters or networks of microcargo that laterally spanned the films (approximately 1 mm). Because microcargo clusters or networks were present before the initiation of flow, minimal coalescence occurred before release. Although some aspects of the LC film behaviors differed from droplets, the studies performed with films provided important insights into clusters formation and how cluster size impacts release of microcargo from the LC.

In the absence of flow, similar to Stage I carrier droplet behavior, microcargo clustering was observed over a period of 10 min (Figure 3c,d). We interpret the clustering process to be driven by relaxation of LC elastic energy associated with the straining of LC around the microcargo, as described in past studies of colloidal assembly processes in LCs.[27] Upon contacting the LC phase with the aqueous surfactant/monomer solution, similar to Stages II-IV (Figure 3e,f, Figure S3, Supporting Information), we observed advective flows to be generated. The interfacial advection observed in the thin LC films and during Stages III and IV of the LC droplet experiments is driven by the partitioning of the LC oil into micelles of surfactant present in the aqueous phase, similar to Stage II. The flow is not driven by a surfactant that is soluble in both the external aqueous phase and the LC carrier droplets, as described by Scriven and Sternling.[35] These flows ultimately resulted in the release of initiator-loaded microcargo into the contacting aqueous phase and the formation of polymer near the LC interface (Figure \$3, Supporting Information). We measured the LC velocity by tracking the displacement of small singly dispersed microcargo. When the initial flow velocity was high (e.g., 120 µms⁻¹), the clusters present during Stage I (200–500 μm) were disrupted by the flow, resulting in a smaller cluster diameter of approximately 50 µm (Figure 3e). In contrast, when the velocity of the LC decreased to 30 µms⁻¹ (Figure 3f, after 4 min), characteristic of Stages III-IV, large clusters (200-500 µm) of a diameter comparable to those observed in the absence of flow were found to form (such large clusters were also observed to be constrained in their motion as the spanned the width of the LC film; see below for additional comments). Figure 3f also reveals that large microcargo (left of the image, red circles) are less likely to cluster under these conditions as compared to small microcargo (red arrow).

The observations above led us to hypothesize that the microcargo cluster size during Stages I–IV is set by a competition between LC elasticity (promoting formation of clusters) and hydrodynamic shear stresses (promoting disruption of clusters). This competition is characterized by the Ericksen number $Er = \eta_{\rm d} v d_0/2 K$, where $\eta_{\rm d}$ is a characteristic viscosity of the LC (80 mPa s), v is flow velocity (10–1000 μ ms⁻¹), d_0 is the diameter of the microcargo, and K is the Frank-Oseen elastic constant of the LC

in the one-constant approximation (7 pN, Experimental Section). For $\nu=20~\mu \rm ms^{-1}$ and $d_0=2~\mu \rm m$, we calculated Er=0.2, indicating that elastic forces dominate (drive formation of large clusters); whereas for either high fluid velocities ($\nu=200~\mu \rm ms^{-1}$ and $d_0=2~\mu \rm m$, Er=2) or large microcargo ($d_0=40~\mu \rm m$ and $\nu=30~\mu \rm ms^{-1}$, Er=6), viscous forces dominate elastic forces and thereby disperse assemblies. This result is consistent with our observation that microcargo increasingly clusters with slowing of the flow velocity within the LC film (Figure 3e,f). It also indicates that small microcargo will cluster before large microcargo as the velocity of the LC decreases, consistent with our observations (Figure 3f).

Additional observations of carrier droplet appearance (Figure S2, Supporting Information) revealed coarsening (growth in size) of individual microcargo during Stage III, which is likely an additional consequence of the circulating flows (Figure 3g). Specifically, the average diameter of microcargo increased from 3.2 \pm 3.5 to 33 \pm 30 μm between Stage I and the end of Stage III (Figure S2, Supporting Information). The coalescence of microcargo was not observed during the absence of flow (Stage I). To understand if flow-driven coalescence underlies our observation of coarsening of aqueous microcargo, we compared the magnitude of short-range colloidal repulsive forces (elastic and electrical double-layer forces) to compressional viscous interactions. We evaluated the contribution of the LC elastic energy to the shortrange repulsive force acting between two microcargo as (Experimental Section): ${}^{[36,37]}F_{\rm e,ss} = -\frac{3}{4}\pi K\zeta^2 \left(\frac{d_0}{d+d_0}\right)^4$, where $\zeta=2.04$ is a constant, K = 7 pN is the elastic constant of the LC, d is the distance that separates the interfaces of the two microcargo. Additionally, an electrical double layer repulsion can be evaluated as (Experimental Section): $^{[23,38,39]}F_{\rm edl,\ ss}=-\frac{8\pi\epsilon_0\epsilon}{\lambda}(\frac{d_1+d_2}{d_1d_2})(\frac{k_BT}{\epsilon_c})^2Y_p^2e^{-\frac{d}{\lambda}},$ where d_1,d_2 are the diameters of the two microcargo, ϵ_0 is the vacuum permittivity, ϵ is the relative permittivity of the LC, λ is Debye screening length, $k_{\rm B}$ is the Boltzmann constant, T is the temperature, e_c is the elementary charge, Y_p is the effective surface potential of the microcargo interface. For $v = 200 \, \mu \text{ms}^{-1}$, $d_0 = d_1 = d_2 = 20 \mu m$ and $d = 1 \mu m$, we calculate viscous forces $(\frac{1}{2}\eta_d v d_0 \approx 160 \text{ pN})$ to be larger than elastic forces ($\approx 56 \text{ pN}$) and electrical double layer forces (\approx 48 pN). In contrast, for $\nu =$ 20 μms⁻¹, viscous forces ($\frac{1}{2}\eta_d v d_0 \approx 16$ pN) are smaller than both elastic forces (≈56 pN) and electrical double layer forces (≈48 pN), indicating that the higher flow velocity can generate viscous forces that are sufficiently large to overcome colloidal repulsions, leading to coalescence. A key conclusion of this analysis is that the Marangoni effect not only drives the motion of the LC carrier droplet (Figure 2), but it also plays a central role in programming size and organization of microcargo clusters that, as we show below, controls their release.

2.3. Mechanism of Release

Initial evidence that cluster size controls release was obtained from observations of microcargo (as clusters) in LC carrier droplets during Stage IV (Figures 2 and 4, Video S2, Supporting Information). The initiator within the microcargo triggered free radical polymerization of monomer in the aqueous solution surrounding the LC carrier droplets to form PNIPAm (polymer),

15214095, 2024, 28, Downloaded from https://onlinelibrary.wiley.com/doi/10.1002/adma.202311311 by Cornell University Library, Wiley Online Library on [22/08/2024]. See the Terms and Conditions (https://onlinelibrary.wiley.com/nerms-and-

conditions) on Wiley Online Library for rules of use; OA articles are governed by the applicable Creative Commons

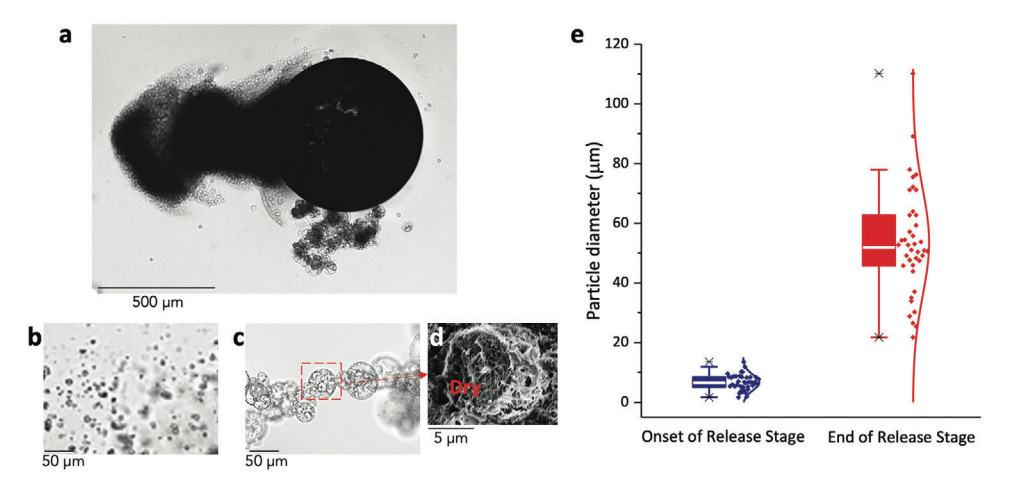


Figure 4. Polymeric microparticles formed by self-timed release of initiator-containing microcargo from liquid crystal (LC) carrier droplets during Stage IV. a) Micrograph showing a trail of polymeric (PNIPAm) particles of various sizes generated upon self-timed release of initiator from a LC carrier droplet. b) Clusters of small polymeric particles were formed initially c) followed by larger polymeric particles. d) Scanning electron microscope (SEM) image of a single polymeric particle (dry). e) Distributions of polymeric particle sizes formed at early and late stages of release of microcargo ($n \ge 5$).

which we characterized by attenuated total reflectance-Fourier transform infrared spectroscopy (ATR-FTIR, Figure S4, Supporting Information). By using bright field microscopy, we observed that the polymer product formed after release of microcargo comprised clusters of discrete polymeric particles (Figure 4a). Additional observations hint that one polymeric particle was generated by the release of one microcargo droplet (see Video \$3, Supporting Information, for the formation of a single bead). We also found that clusters of small polymeric particles (Figure 4b, 6.6 \pm 2.5 µm) formed before clusters of large particles (Figure 4c,d, $53.6 \pm 17.6 \,\mu\text{m}$), consistent with our observations in Figure 3f and scaling analysis indicating that microcargo with small sizes form clusters before large ones within the LC carrier droplet. Overall, the cluster-like structure of the polymeric particles (of either small or large particles, Figure 4a-c) was found to mirror the microcargo clusters observed under the influence of flow within the LC phase (Figure 3). This correspondence led us to hypothesize that clustering plays a role in the autonomous release of the microcargo from the LC carrier droplets.

We further explored the process leading to release of microcargo by making microscopic observations at the interface of the LC film in contact with the surfactant/monomer solution (Figure 5, Video S4, Supporting Information). We note Figure 5 was obtained using the film ($\approx 100~\mu m$ thickness) geometry. In the film geometry, clusters that form with a size larger than the LC film thickness will be restricted in their motion due to interactions with the confining surfaces. This is evident in Figure S6a (Supporting Information) where the very largest clusters are not transported toward the interface. The constraining effect of LC film thickness means that the largest clusters that were observed in the vicinity of the LC interface were approximately equal to the LC film thickness ($\approx 100~\mu m$ in thickness).

Through microscopic observations using this experimental setup, we found that under high shear conditions (fluid velocity $\approx \! 100 \ \mu ms^{-1}$), small individually dispersed microcargo (<25 μm) and clusters carried by the flow within the LC film were reflected from the LC interface rather than released (Figure 5a). Con-

versely, larger microcargo ($\approx50~\mu m$) and clusters of microcargo ($\approx100~\mu m$) tended to be ejected through the LC interface into the surrounding aqueous phase (Figure 5a,b,d–f and Figure S7, Supporting Information). Even when fluid velocities decreased to 10–20 μms^{-1} (low shear conditions), large clusters (200–300 μm in diameter) or aggregates of multiple clusters were still observed to trigger release events (Figure 5c, Figures S7 and S8, Supporting Information). When combined, these observations led us to hypothesize that hydrodynamic stresses associated with large clusters are sufficient to trigger the escape of microcargo from the LC (Figure 5d–f, discussed below).

Accompanying the release of a cluster, we also observed a local transient increase in flow strength (Video S4, Supporting Information), which appeared to feed back into the release of additional clusters (Figure 5f). We interpret the transient increase of flow velocity to likely arise from reinforcement of the Marangoni stress generated by the transfer of surfactant from within microcargo onto the LC interface.

In the absence of sufficiently large hydrodynamic stresses, we propose that repulsive forces act on the microcargo clusters near the aqueous interface of the LC carrier droplets to prevent release, and that the forces arise from elastic, $F_{\rm e,si}$, and electrical double layer interactions, $F_{\rm edl,\,si}$ (see Figure S5, Supporting Information and Experimental Section for calculations). Evaluation of these repulsive colloidal forces acting on the microcargo clusters ($F_{\rm R} = F_{\rm e,si} + F_{\rm edl,\,si}$ and Figure S5, Supporting Information) reveals that they scale approximately with the size of the cluster $F_{\rm R} = \alpha D_{\rm c}$, where α is a scalar and $D_{\rm c}$ is the diameter of a cluster, as electrical double layer forces dominate for large clusters. The associated stress scales as $\sigma_{\rm R} = F_{\rm R}/D_{\rm c}^2 = \alpha/D_{\rm c}$.

We consider the hydrodynamic stresses that trigger release to comprise both viscous σ_v and inertial σ_1 components. In our experiments, the inertial contribution to hydrodynamic stresses at the level of single microdroplets (microcargo) is unlikely to be important, but this may not be true for clusters. [40] In such a scenario, the inertia is associated with the size of the cluster and not the individual microcargo droplets. To estimate the relative importance of inertial and viscous stresses, we define the Reynolds

1521495, 2024, 28, Downoladed from https://onlinelbray.aviley.com/doi/10.1002/adma.20211111 by Cornell University Library, Wiley Online Library on [22082024], See the Terms and Conditions (https://onlinelibray.aviley.com/terms-and-conditions) on Wiley Online Library for rules of use; OA articles are governed by the applicable Creative Commons Licenses

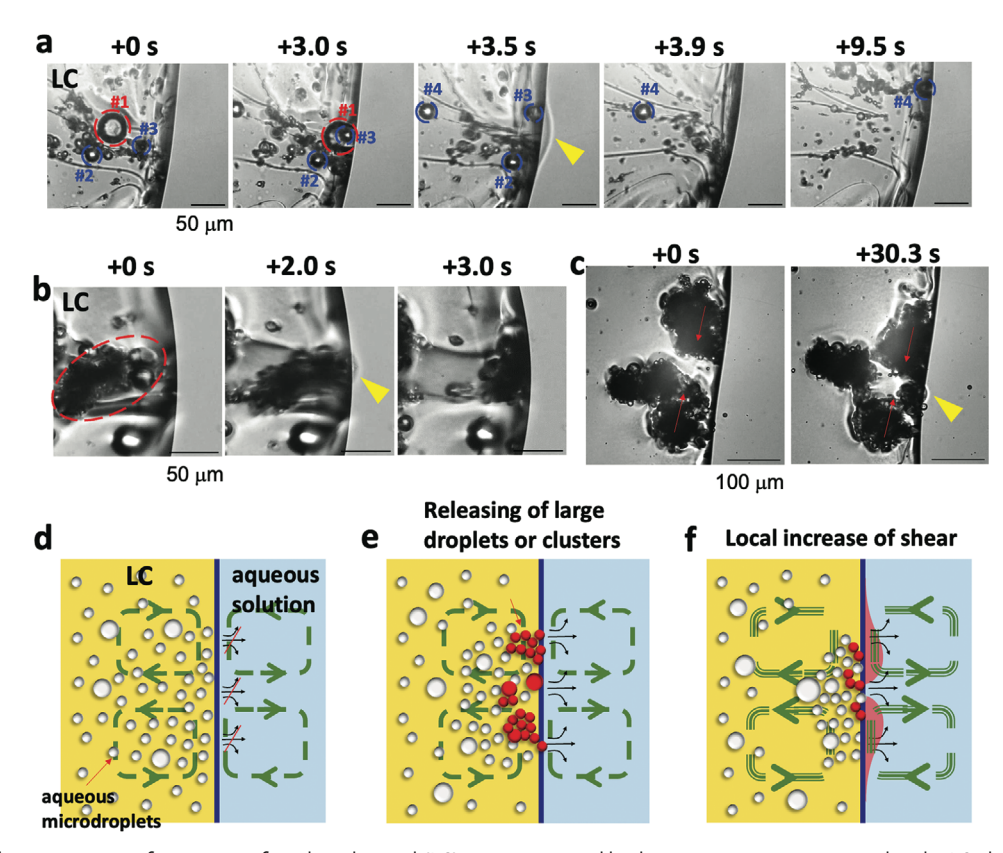


Figure 5. Hydrodynamic escape of microcargo from liquid crystal (LC) as programmed by dissipative processes internal to the LC phase. a) Micrographs showing that high shear conditions (fluid velocity $\approx 100~\mu ms^{-1}$) cause small singly dispersed microcargo (circled in blue) to be reflected back into the LC by interactions with the LC interface, while large microcargo (circled in red) are released. b) Micrographs show that a large cluster of microcargo (circled in red) moving toward the LC interface is subjected to a sufficiently large hydrodynamic force, allowing it to pass through the interface and enter the surrounding aqueous phase. c) Micrographs show that assembly of two clusters of microcargo into a large cluster under low shear conditions (fluid velocity $\approx 20~\mu ms^{-1}$) can lead to release of microcargo. Yellow arrows indicate location of release of the clusters. Red arrows denote motion of clusters in c). d-f) Schematic illustrations of the proposed mechanism. Green arrows indicate fluid flow. Black arrows indicate release of microcargo. d) Small clusters and single microcargo cannot overcome the repulsive colloidal barrier from the interface, while e) large microcargo and clusters of microcargo possess sufficient momentum to overcome the repulsion. f) The surfactant released from the microcargo accelerates advection by reinforcing the Marangoni effect, promoting further release.

number based on cluster size as follows $Re_{cluster} = \frac{\rho_c \dot{\gamma} D_c^2}{\eta}$, where ρ_c ($\approx 10^3$ kg m⁻³) is the average density of the cluster, $\dot{\gamma}$ is an average shear rate of the flow experienced by the cluster, D_c is the diameter of the cluster, and η ($\approx 10^{-3}$ Pa s) is a characteristic viscosity of the liquid crystal. Although it is challenging to provide exact estimates of the shear rate $\dot{\gamma}$, our observations of tracer particles in multiple videos lead us to estimate that the flow velocity ranges (in order of magnitude) from 1 to 100 µms⁻¹, and that the sizes of local vortices near the interface range from 10 to 100 μm, as illustrated in Figure S6 (Supporting Information). Cluster size distributions observed in our droplet experiments are also broad, ranging from 10 to 1000 µm. Accordingly, the shear rate $\dot{\gamma}$ (velocity/vortex size) is estimated to range from 0.01 to 10 $\ensuremath{\mathrm{s}^{-1}}$, and for clusters with sizes of 10–1000 μm , Re_{cluster} ranges from 10⁻⁶ to 10. Although the Re_{cluster} is calculated to be much smaller than unity for small cluster sizes and low shear rates, for large clusters and high shear rates, the Re_{cluster} is 10, indicating that it is possible that inertial hydrodynamic stresses are important. We evaluate the hydrodynamic stresses

as follows: $[^{41-45}] \sigma_h = \sigma_v + \sigma_I \sim \eta \dot{\gamma} (1 + D_c^3 n_c) + \rho_c \dot{\gamma}^2 D_c^2 (1 + D_c^3 n_c),$ where n_c is the number density of clusters, and $D_c^3 n_c$ is related to the local volume ratio of microdroplets in LC (overall volume ratio of microdroplets in LC is $\leq 10\%$). The first term combines the viscous stress from the LC and dissipation from the presence of the clusters. The second term represents both the inertia of the clusters and the added inertia from the microdroplets joining the clusters (Supporting Information). We propose that the release of clusters occurs when the hydrodynamic stresses overcome the repulsive colloidal stresses (i.e., $\sigma_R = \alpha/D_c$). Hydrodynamic stresses scale with D_c^2 or D_c^5 , whereas repulsive colloidal stresses scale with D_c^{-1} . Therefore, larger cluster sizes or higher shear rates favor the release of microcargo. This analysis is consistent with our experimental observations (Figure 5a-c, Figures S6-S8, Supporting Information). Additional characterization of the size and shape distributions of microcargo and clusters, as well as the shear rate profile across the sample, is necessary for quantitative analysis of hydrodynamic stresses to determine if the hydrodynamic stresses driving release are viscous or inertial in

15214095, 2024, 28, Downloaded from https://onlinelbray.wiley.com/doi/10.1002/adma.20211311 by Cornell University Library. Wiley Online Library on [2208/2024]. See the Terms and Conditions (https://onlinelibray.wiley.com/terms-and-conditions) on Wiley Online Library for rules of use; OA articles are governed by the applicable Creative Commons Licenses

nature (indeed, they may well cross-over as the size of the clusters increases to the LC droplet size).

The results above, when combined, reveal that the presence of both flow and large clusters of microcargo generates hydrodynamic forces of sufficient magnitude that they can overcome the repulsive colloidal forces that trap the microcargo in the LC carrier droplets and thereby trigger microcargo release (Figure 1a-d). During Stage I, although large clusters form via LC-mediated elastic attractions, the absence of flow leaves the clusters trapped inside the carrier droplet by the colloidal forces. In contrast, in Stage II, the presence of strong internal flows within the LC carrier droplets generates hydrodynamic forces that are sufficient to break up clusters and hence unable to generate large microstructures (clusters) with sufficient hydrodynamic stress that can overcome colloidal interactions at the surface of the LC carrier droplets (Figure S6, Supporting Information). It is only after Stage II, when the flow diminishes sufficiently for clusters to reform (Stage III), that microcargo clusters can escape the LC carrier droplets (Stage IV). This sequence of events is controlled by dissipative processes occurring within the droplet, leading to the self-timed release of microcargo at a targeted location.

Overall, our study identifies a set of conditions involving elastic, colloidal, and hydrodynamic forces under which clusters of droplets can escape from the LC. We note that release of microcargo is not determined by the magnitude of the imposed surfactant concentration gradient (large or small) but rather by the flow generated internally to the LC droplets. We also comment that the balance of elastic, colloidal, and hydrodynamic forces that lead to release occurs in a defined set of experimental conditions, thus providing control over when release occurs. We show that those conditions can be engineered in several geometries in our paper – the self-propelled droplets, the films, and the millifluidic channel described below.

2.4. Self-Regulated Delivery in Millifluidic Channel

Ballistic colloids directed of active motions chemotaxis^[15,25,26,46–48] or electric potentials^[49] have been used to find the shortest path through complex structures, such as a maze[15,25,46,49] and also used to perform logic functions within binary branched channels.[15,47] To show how autonomous triggering of polymerization can follow chemotactic navigation of droplets to a targeted location in a complex environment, we designed a millifluidic channel system with a main channel that splits into three branches (Figure 6, Video S5, Supporting Information). By generating a chemical gradient of surfactant and monomers in branch 3, the LC carrier droplet was guided into this branch undergoing ballistic motion for 3-4 min. After another minute of reorganization, initiator microcargo were autonomously released, and subsequently polymerization was triggered in the channel. The carrier droplet and the resulting polymer product blocked the channel branch (Figure 6, Video S5, Supporting Information). Overall, this result demonstrates that the chemotactic droplets can au-

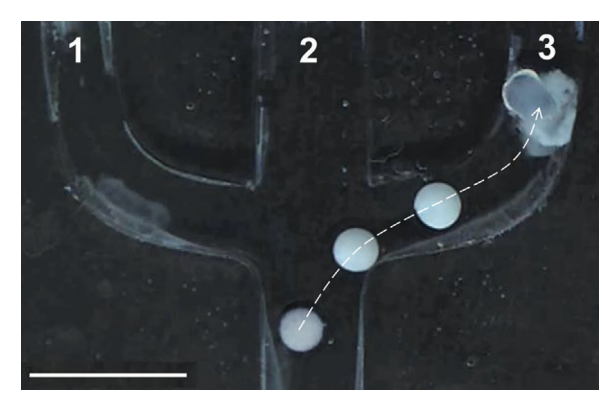


Figure 6. Self-timed and spatially targeted delivery of microcargo within a millifluidic channel that leads to formation of a polymeric plug. Time-lapse images showing a liquid crystal (LC) carrier droplet (white) navigating a three-way branch in a millifluidic channel using a chemical gradient of surfactant and monomer, and subsequent self-timed release of microcargo containing an initiator for polymerization that leads to formation of a polymeric plug in the channel. The LC carrier droplet was initially in 5×10^{-3} M SDS aqueous solution; a concentrated solution (1 M SDS, 30 wt% monomers, monomer:cross-linker = 100:1, 1 vol% catalyst) was injected into branch 3 to create the chemical gradient that caused chemotaxis of the LC carrier droplet. White dashed line indicates the trajectory of the LC carrier droplet. Scale bar, 5 mm.

tonomously delivery microcargo to locations targeted by chemical gradients.

3. Conclusion

In summary, our results demonstrate how dissipative processes within soft matter can be used to program time- and spacedependent functional behaviors. Specifically, we demonstrate these principles by using self-propelled droplets for autonomous delivery of reactive species (initiator) to targeted locations (source of chemoattractant) via a self-timed release process. Marangoni stresses, which drive the ballistic motion of the droplets, also generate internal viscous forces which create microstructures (clusters) with sufficient hydrodynamic forces that compete with colloidal forces to control the nonequilibrium organization of microcargo in ways that time microcargo release. The principles, however, are general, and can be applied to a broad range of soft matter systems that are undergoing convection or advection driven by dissipative processes. Additionally, in the context of the example presented in this paper, a wide range of active chemical species can be loaded into aqueous microcargo, including pharmaceutical compounds,[50] antibacterial agents,[23] and essential nutrients, [20,51] allowing their release to be programmed via design of dissipative processes. Finally, we envisage the use of external stimuli, such as magnetic or electric fields, [52] thermal signaling,[23] interfacial enzymatic events,[53] and bacterial shear forces, [23] all of which have been used in past studies to modulate LCs, to further diversify the functional properties that can be programmed by harnessing dissipative processes within soft matter system. In the long term, these principles may enable fresh approaches to the creation of miniature machines and robotics that

www.advancedsciencenews.com



www.advmat.de

can perform complex tasks such as targeted disease therapies, environmental monitoring, or small-scale fabrication. The ability to incorporate nonequilibrium strategies in functional soft materials designs may also enable the development of new chemical and biomolecular technologies (e.g., for flow chemistry).

4. Experimental Section

Materials: Nematic LC E7 was purchased from HCCH (Jiangsu Hecheng Display Technology Co., Ltd). N-Isopropylacrylamide (NIPAm, 97%, monomer), N,N'-methylenebis (acrylamide) (BIS, cross-linker), ammonium persulfate (APS, initiator), N,N,N',N'-tetramethylethylenediamine (TEMED, catalyst), sodium dodecyl sulfate (SDS), and Rose Bengal (water-soluble fluorescent dye) were purchased from Sigma—Aldrich. The dye monomer methacryloxyethyl thiocarbamoyl rhodamine B was purchased from Polysciences. Fisher Finest Premium Grade glass slides were purchased from Fisher Scientific. Purification of water (18.2 M\Omega cm resistivity at 25 °C) was performed using a Milli-Q water system (Millipore, Bedford, MA, USA).

Preparation of w/o/w LC Double Emulsions Containing Aqueous Initiator Microcargo: First, surfactant SDS (5×10^{-3} M) and initiator APS (10 wt%) were dissolved into MilliQ water. The density of the APS–SDS aqueous phase was measured to be 1.05 g cm $^{-3}$, slightly higher than the density of E7 of 1.03 g cm $^{-3}$. Next, the resulting solution was emulsified into LC oil at 1.10 ratio by vortexing for 1 min at 3000 rpm. The LC oil used was a nematic phase E7, a eutectic mixture of four mesogens with a LC temperature range from below room temperature to 60 °C. This composition was selected because it remains a LC phase under all conditions reported in this paper. The last step was adding the oil mixture into SDS solution (5×10^{-3} M) at 0.5-1:10 ratio, and gently shaking the solution to form double emulsions.

Preparation of Surfactant/Monomer Solution: First, surfactant SDS (1 M) was dissolved into MilliQ water by vortexing and heating to 60 °C for 2 h to facilitate the process (SDS micellar solution). Second, monomers (10–30 wt%, NIPAm: BIS = 100:1 wt) were dissolved into the SDS micellar solution. Third, catalyst TEMED (1 vol%) was added into the aqueous phase to make the final micellar solution. This reaction was selected because of its rapid nature. Upon mixing macroscopic volumes of initiator, catalyst, and monomer, polymerization was observed within a few seconds of mixing.

Chemotactic LC Carrier Droplet Triggering Polymerization Experiment: Glass slides were first washed using ethanol and water. Optical cells were assembled from two 25 \times 25 mm glass slides separated from each other by 1–2 mm-thick spacers. The double emulsion solution was subsequently injected from one end of the optical cell, and the surfactant/monomer solution from the other end of the cell to induce the contacting of the two solutions. The experiments were done at an elevated temperature of 35 $^{\circ}$ C using a Linkam hot stage. The behaviors of the double emulsion droplets were recorded using a Canon EOS Rebel T6i camera at 30 fps with a Canon EF-mount 105 mm f/2.8 EX DG OS HSM Macro lens or under polarized light microscopy. The droplet positions were extracted and analyzed using Image).

Observation of Microcargo Coalescence and Clustering in Thin Films: A total of 15 X 12 mm optical cells were assembled from two glass slides separated from each other by $\approx 100 \ \mu m$ -thick spacers. SDS (5 \times 10⁻³ M) and initiator APS (10 wt%) were dissolved into MilliQ water. The resulting solution was emulsified into E7 at 1:10-1:100 ratio by vortexing for 1 min at 3000 rpm. The oil mixture was subsequently injected from one end of the optical cell, and the surfactant/monomer solution (0.8-1 м SDS, 5 wt% monomers, NIPAm: BIS = 100:1 wt, 1 vol% TEMED) from the other end of the cell to induce the contacting of the two fluid phases. It was noted that a low monomer concentration (5 wt%) was used in these experiments to slow polymerization and thus enable observation of the release process over an extended duration. The experiments were done at an elevated temperature of 35 °C using a Linkam hot stage. The behaviors of the initiator microcargo were recorded under polarized light microscopy, and were processed and analyzed using ImageJ. Here, the initiator-to-monomer ratio was higher than that used in the LC carrier droplet experiments, and this difference was observed to cause a polymer film rather than polymeric particles to form at the LC interface (Figure S3, Supporting Information).

Fabrication of Millifluidic Channel: Millifluidic channels of thickness 1.6 mm were printed on a laser cutter (Zing 40 watt; Epilog Laser) from a piece of acrylic sheet. Acrylic covers were also printed on the laser cutter. A set of acrylic cover and channel was bound together by dropping chloroform on the surfaces, and pressing the surfaces to contact until chloroform evaporated (≈2 min). The channel was then glued onto a glass substrate using epoxy resin, and coated with poly(vinyl alcohol) (PVA) to make the channel hydrophilic. The droplet experiments were done at an elevated temperature of 40–45 °C on the hot stage.

Zeta Potential Measurements: A total of 0.1 μ L E7 was homogenized for 30 s into 10 mL water. An amount of 240 μ L of LC-in-water emulsion was then diluted in 10 mL of either water or 5 \times 10⁻³ $\,$ M SDS. After allowing 30 min for the sample to equilibrate, zeta potentials on the aqueous side of the LC-aqueous interface were measured using a Malvern Zetasizer Nano instrument. Data were averaged over five consecutive runs.

Attenuated Total Reflectance Fourier Transform Infrared Spectroscopy (ATR–FTIR): The polymer pieces (PNIPAm) from the chemotactic LC droplet experiments were taken out and washed with water and ethanol, and dried under ambient conditions for more than 5 days. [54,55] NIPAm monomer (dry) and dried PNIPAm samples from the chemotactic LC carrier droplet experiments were ground and then compressed into disks before testing. Infrared spectroscopy analysis was done using a Bruker Vertex V80V vacuum FTIR system, equipped with an ATR accessory, in the 4000–600 cm⁻¹ spectral range.

Scanning Electron Microscope (SEM): For SEM characterization of polymer beads, the polymers were immersed in ethanol for 48 h and dried under a stream of nitrogen to extract remaining LCs, water, and unreacted monomers. Following the extraction, imaging of the morphology of the polymer networks was performed by Zeiss Gemini 500 Scanning Electron Microscope

Trapping and Segregation of Initiator Microcargo: Initiator microdroplets (microcargo) in LCs are sequestered within the LC bulk phase by the elastic energies associated with the strain of orientational ordering of LCs around the microdroplets. [56,57] Assuming one elastic constant K, the elastic energy depends on microdroplet diameter d_0 (Kd_0 , typical $K=10^{-11}$ N), which competes with surface anchoring energy (Wd_0^2 , where $W=10^{-5}$ N m⁻¹ is anchoring energy density). [58] A microdroplet suspended in LC with diameter $d_0 > K/W = 1 \, \mu m$ (that is $Wd_0^2 > Kd_0$) generates elastic repulsion that prevents coalescence with other droplets.

Estimation of Elastic Constant for E7: It was found that monomers can diffuse into E7, which decreases the elastic constant. To estimate the elastic constant, E7 was equilibrated with 10 wt% NIPAm solution at 35 °C for 5 h, and then the nematic to isotropic phase transition temperature of the E7 phase was measured to be 50 °C, 10 °C lower than pure E7. Elastic constant ($K = K_{11}$) of pure E7 at 30 °C was reported to be 9–10 pN; and 4–8 pN at 40 °C.[59,60] The elastic constant was estimated as K = 7 pN. A change in the value of K from 4 to 10 pN did not change the conclusions of the model.

Interplay Between Hydrodynamic and Elastic Forces: It is noted that elastic forces arising from LC ordering interact with flows on length scales of tens of micrometers (see scaling analysis in the main text). For LC droplets with diameters of tens of micrometers, the interplay of elastic and hydrodynamic forces can lead to curly droplet trajectory, but for large carrier droplet (1 mm) studied here, the dominant effect of internal flow is to reorganize the microcargo. The interplay of hydrodynamic and elastic forces also underlies the flow-triggered release of microcargo described in the paper. The release behavior could be further tuned by engineering these forces. For example, to slow the rate of release of cargo, one strategy could be to decrease the strength of the elastic forces – this will slow the clustering process and thus slow the fraction of microdroplets present in clusters of sufficient size that they can escape the LC.

Calculation of Elastic and Electrical Double layer Interactions: The interplay of elastic and electrical double layer forces plays a key role in the creation of an energetic barrier that hinders the release of microcargo from the LC droplets. In the evaluation of this energetic barrier, as detailed below, the energetic barrier encountered during the transport of the cluster

1521405, 2024, 28, Downloaded from https://onlinelbray.wiley.com/doi/10.1002/adma.20211311 by Cornell University Library, Wiley Online Library on [22008/2024]. See the Terms and Conditions (https://onlinelibray.wiley.com/terms-and-conditions) on Wiley Online Library for rules of use; OA articles are governed by the applicable Creative Commons Licenses

5214095, 2024, 28, Downloaded from https://onlinelibrary.wikey.com/doi/10.1002/adma.202311311 by Cornell University Library, Wiley Online Library on [22/082024]. See the Terms and Conditions (https://onlinelibrary.wikey.com/terms

toward the interface was calculated. This process is assumed to not involve a change in interfacial area, and thus interfacial tension does not enter into the model. However, once the cluster is inserted into the interface, the interfacial tension will have a large impact on the path energetics. This contribution will be favorable and will drive the process rapidly forward.

The elastic repulsion between the LC-bulk aqueous interface and microcargo clusters was evaluated as:[23,38,61]

$$F_{e,si} = -A\pi K\zeta^2 \left(\frac{D_c}{2h + D_c}\right)^4 \tag{1}$$

where A is a constant that is dependent on anchoring (3/4 for planar anchoring, where mesogens are parallel to interface, and 1/2 for homeotropic anchoring, where mesogens are perpendicular to interface (this work), respectively), $\zeta = 2.04$ is a constant, K is a characteristic LC elastic constant, D_c (>K/W) is the diameter of the microcargo cluster, h is the distance of the cluster surface from the LC-bulk aqueous interface. It is noted that Equation (1) was developed to describe the long-range interaction between particles and interfaces for the case where the particles carry hyperbolic point defects. [62-64] The scaling laws developed for long-range interactions, however, have also been found to describe the experimental characterization of the interactions of particles at close approach (i.e., $h < D_c$). [62–64] For 2 μm microdroplet/cluster near the interface (h=0) and homeotropic anchoring of E7 at water interface, $F_{\rm e,si}$ is evaluated to be 6.5 \times 10⁻¹¹ N, which is large compared to gravitational forces $F_{\rm g} =$ 8 \times 10⁻²² N ($\Delta \rho g \times \frac{4}{3}\pi \times \frac{1}{8}D_c^3$, where $\Delta \rho = 2 \times 10^{-5}$ kg m⁻³ is the density difference between aqueous droplet and E7, g = 9.81 m s⁻² is the gravitational acceleration).

Similarly, the forces generated by the LC elasticity between two microcargo spheres were evaluated as:[28,37,38]

$$F_{\text{e,ss}} = -\frac{3}{4}\pi K\zeta^2 \left(\frac{d_0}{d+d_0}\right)^4 \tag{2}$$

where d_0 is the diameter of microcargo, d is the distance that separates the interfaces of the two microcargo.

Other interactions, such as electrostatic attractions, can reinforce the trapping of microcargo.^[23] Electrical double-layer interactions exist between negative charges at the LC-bulk aqueous interface and the negatively charged SDS on the interface of microcargo, thus generating repulsions. The forces generated by the electrical double-layer interactions between the cluster sphere and the interface were evaluated as:[23,39,65]

$$F_{\text{edl, si}} = -2\pi\varepsilon_0 \varepsilon \frac{D_c}{\lambda} \left(\frac{k_B T}{e_c}\right)^2 Y_p Y_i e^{-\frac{h}{\lambda}}$$
(3)

where ϵ_0 is vacuum permittivity, ϵ is the relative permittivity of the LC (for E7 with homeotropic anchoring $\epsilon_{\parallel}=$ 19; for planar anchoring $\epsilon_{\perp}=$ 5.2), [66] λ is the Debye screening length, $k_{\rm B}$ is the Boltzmann constant, T is temperature, $\emph{e}_\emph{c}$ is the elementary charge, $\emph{Y}_\emph{p}$ is the effective surface potential of the microcargo, Yi is the effective surface potential of the LC-bulk aqueous interface, and the negative sign — means repulsion. λ , $Y_{\rm p}$, and $Y_{\rm i}$ can

$$\lambda = \sqrt{\frac{\varepsilon_0 \varepsilon k_B T}{2e_c^2 N_A I}} \tag{4}$$

$$Y_{p} = \frac{8 \tanh\left(\frac{D\zeta_{p}e_{c}}{k_{B}T}\right)}{1 + \sqrt{1 - \frac{\left(\frac{D_{c}}{\lambda}\right) + 1}{\left(\left(\frac{D_{c}}{2\lambda}\right) + 1\right)^{2}} \tanh^{2}\left(\frac{D\zeta_{p}e_{c}}{k_{B}T}\right)}}$$
(5)

$$Y_{i} = 4 \tanh \left(\frac{D\zeta_{i}e_{c}}{k_{B}T} \right) \tag{6}$$

where $N_A = 6.02 \times 10^{23}$ is the Avogadro constant, I is ionic strength of LC, D is a constant, ζ_p and ζ_i are zeta potentials at the microcargo surface and LC-aqueous interface, respectively.

In the presence of anionic surfactant SDS, $A=\frac{1}{2}$, K=7 pN, $\epsilon_0=8.854\times 10^{-12}$ C V $^{-1}$ m $^{-1}$, $\epsilon=\epsilon_{\parallel}=19$, $k_{\rm B}=1.38\times 10^{-23}$ J K $^{-1}$, T=308.15 K, $e_c=1.602\times 10^{-19}$ C, $I=1.8\times 10^{-5}$ mol m $^{-3}$, D is between 1 to 8, [67] $\zeta_{\rm p}=-66.25$ mV, $\zeta_{\rm i}=-66.25$ mV, and $\lambda=0.89$ $\mu{\rm m}$. For $D_{\rm c}=$ 6 μ m, cluster at h=2 μ m, this work calculated $F_{\rm e,si}=-1.54$ pN, $F_{\rm edl, si}=$ -6.89 pN, and thus the net force $F_{\text{net}} = F_{\text{e,si}} + F_{\text{edl, si}} = -8.43$ pN, which indicates repulsion from LC interface. This work notes that $F_{\text{net}} = 10^{10} F_{\text{g}}$ as described above, so gravity is negligible for droplets near the E7-bulk aqueous phase interface.

Similarly, this work evaluates the forces generated by the electrical double-layer interactions between two microcargo spheres as:[23,39]

$$F_{\text{edl, ss}} = -\frac{8\pi\epsilon_0 \varepsilon}{\lambda} \left(\frac{d_1 + d_2}{d_1 d_2}\right) \left(\frac{k_\text{B} T}{e_c}\right)^2 Y_\text{p}^2 e^{-\frac{d}{\lambda}} \tag{7}$$

where d_1 , d_2 are the diameters of the two spheres, Y_p obtained with $\frac{\frac{1}{2}d_1+\frac{1}{2}d_2}{\frac{1}{2}d_1\cdot\frac{1}{2}d_2}$ replacing $\frac{1}{2}D_c$ in Equation (5), d is the distance separating the interfaces of the two spheres, and the negative sign – means repulsion. For $d_1 = d_2 = 3 \mu \text{m}$, $d_1 = 1 \mu \text{m}$, this work calculates $F_{\text{edl, ss}} = -10.60 \text{ pN}$; and for $d_1 = d_2 = 30 \,\mu\text{m}$, $d_1 = 1 \,\mu\text{m}$, $F_{\text{edl, ss}} = -70.10 \,\text{pN}$, approximately one order of magnitude larger compared to the small microcargo.

Supporting Information

Supporting Information is available from the Wiley Online Library or from the author

Acknowledgements

This work was primarily funded by the Army Research Office through W911NF-15-1-0568 and W911NF-17-1-0575. Additional support was received from the National Science Foundation through IIS-1837821, DMR-1921722 and DMR-2003807. S.H. acknowledges financial support from the National Science Foundation through CBET-2210322.

Conflict of Interest

The authors declare no conflict of interest.

Data Availability Statement

The data that support the findings of this study are available from the corresponding author upon reasonable request.

Keywords

active materials, autonomous micromachines, dissipative processes, spatiotemporal programming

> Received: October 27, 2023 Revised: February 12, 2024 Published online: May 13, 2024

[1] E. P. Solomon, L. R. Berg, D. W. Martin, Biology, 9th ed., Boorks/Cole, Cengage Learning, Boston, MA 2011.

on Wiley Online Library for rules of use; OA articles are governed by the applicable Creative Commons License

.5214095, 2024, 28, Downloaded from https://onlinelibrary.wiley.com/doi/10.1002/adma.202311311 by Cornell University Library, Wiley Online Library on [22/08/2024]. See the Terms

and Conditions (https://onlinelibrary.wiley

on Wiley Online Library for rules of use; OA articles are governed by the applicable Creative Commons

- [2] Y. Rikitake, Y. Takai, Int. Rev. Cell Mol. Biol. 2011, 287, 97.
- [3] C.-M. Lo, H.-B. Wang, M. Dembo, Y.-L. Wang, Biophys. J. 2000, 79, 144
- [4] K. Ley, C. Laudanna, M. I. Cybulsky, S. Nourshargh, Nat. Rev. Immunol. 2007, 7, 678.
- [5] W. He, S. Holtkamp, S. M. Hergenhan, K. Kraus, A. de Juan, J. Weber, P. Bradfield, J. M. P. Grenier, J. Pelletier, D. Druzd, C.-S. Chen, L. M. Ince, S. Bierschenk, R. Pick, M. Sperandio, M. Aurrand-Lions, C. Scheiermann, *Immunity* 2018, 49, 1175.
- [6] B. Bénazéraf, P. Francois, R. E. Baker, N. Denans, C. D. Little, O. Pourquié, *Nature* 2010, 466, 248.
- [7] S. J. Streichan, M. F. Lefebvre, N. Noll, E. F. Wieschaus, B. I. Shraiman, Elife 2018, 7, e27454.
- [8] T. Sanchez, D. T. N. Chen, S. J. Decamp, M. Heymann, Z. Dogic, Nature 2012, 491, 431.
- [9] A. Bricard, J. B. Caussin, N. Desreumaux, O. Dauchot, D. Bartolo, Nature 2013, 503, 95.
- [10] M. C. Marchetti, J. F. Joanny, S. Ramaswamy, T. B. Liverpool, J. Prost, M. Rao, R. A. Simha, *Rev. Mod. Phys.* 2013, 85, 1143.
- [11] M. M. Hanczyc, T. Toyota, T. Ikegami, N. Packard, T. Sugawara, J. Am. Chem. Soc. 2007, 129, 9386.
- [12] T. Toyota, N. Maru, M. M. Hanczyc, T. Ikegami, T. Sugawara, J. Am. Chem. Soc. 2009, 131, 5012.
- [13] Z. Izri, M. N. van der Linden, S. Michelin, O. Dauchot, Phys. Rev. Lett. 2014, 113, 248302.
- [14] S. Herminghaus, C. C. Maass, C. Krüger, S. Thutupalli, L. Goehring, C. Bahr, Soft Matter 2014, 10, 7008.
- [15] C. Jin, C. Krüger, C. C. Maass, Proc. Natl. Acad. Sci. U. S. A. 2017, 114, 5089
- [16] X. Wang, R. Zhang, A. Mozaffari, J. J. de Pablo, N. L. Abbott, Soft Matter 2021, 17, 2985.
- [17] C. H. Meredith, P. G. Moerman, J. Groenewold, Y. J. Chiu, W. K. Kegel, A. van Blaaderen, L. D. Zarzar, Nat. Chem. 2020, 12, 1136.
- [18] C. Krüger, G. Klös, C. Bahr, C. C. Maass, Phys. Rev. Lett. 2016, 117, 048003.
- [19] B. V. Hokmabad, K. A. Baldwin, C. Krüger, C. Bahr, C. C. Maass, Phys. Rev. Lett. 2019, 123, 178003.
- [20] M. Li, M. Brinkmann, I. Pagonabarraga, R. Seemann, J.-B. Fleury, Commun. Phys. 2018, 1, 23.
- [21] B. Esteban-Fernández De Ávila, D. E. Ramírez-Herrera, S. Campuzano, P. Angsantikul, L. Zhang, J. Wang, ACS Nano 2017, 11, 5367
- [22] M. Hansen-Bruhn, B. E. F. de Ávila, M. Beltrán-Gastélum, J. Zhao, D. E. Ramírez-Herrera, P. Angsantikul, K. Vesterager Gothelf, L. Zhang, J. Wang, Angew. Chem., Int. Ed. 2018, 57, 2657.
- [23] Y.-K. Kim, X. Wang, P. Mondkar, E. Bukusoglu, N. L. Abbott, *Nature* 2018, 557, 539.
- [24] X. Wang, H. Sun, Y.-K. Kim, D. B. Wright, M. Tsuei, N. C. Gianneschi, N. L. Abbott, Adv. Mater. 2022, 34, 2106535.
- [25] I. Lagzi, S. Soh, P. J. Wesson, K. P. Browne, B. A. Grzybowski, J. Am. Chem. Soc. 2010, 132, 1198.
- [26] S. Zhang, C. Contini, J. W. Hindley, G. Bolognesi, Y. Elani, O. Ces, *Nat. Commun.* 2021, 12, 1673.
- [27] I. Muševič, M. Škarabot, U. Tkalec, M. Ravnik, S. Žumer, *Science* **2006**,
- [28] P. Poulin, D. A. Weitz, Phys. Rev. E 1998, 57, 626.
- [29] R. C. Ball, J. R. Melrose, in *Proc. INDO-U.K. Forum*, Imperial College Press, London 1996, pp. 396–405.
- [30] J. R. Melrose, R. C. Ball, Europhys. Lett. 1995, 32, 535.
- [31] R. S. Farr, J. R. Melrose, R. C. Ball, Phys. Rev. E 1997, 55, 7203.

- [32] B. Andreotti, Y. Forterre, O. Pouliquen, Granular Media: Between Fluid and Solid, Cambridge University Press, Cambridge 2013.
- [33] R. Mari, R. Seto, J. F. Morris, M. M. Denn, J. Rheol. 2014, 58, 1693.
- [34] N. J. Wagner, J. F. Brady, Phys. Today 2009, 62, 27.
- [35] C. V. Sternling, L. E. Scriven, AIChE J. 1959, 5, 514.
- [36] P. Poulin, H. Stark, T. C. Lubensky, D. A. Weitz, Science 1997, 275, 1770.
- [37] O. P. Pishnyak, S. Tang, J. R. Kelly, S. V. Shiyanovskii, O. D. Lavrentovich, Phys. Rev. Lett. 2007, 99, 127802.
- [38] P. C. Hiemenz, R. Rajagopalan, Principles of Colloid and Surface Chemistry, CRC Press, Boca Raton 1997.
- [39] J. N. Israelachvili, Intermolecular and Surface Forces, Academic Press, San Diego, CA 2011.
- [40] Y. Madraki, A. Oakley, A. Nguyen Le, A. Colin, G. Ovarlez, S. Hormozi, J. Rheol. 2020, 64, 227.
- [41] S. Hormozi, presented at Gordon Research Conf. Particulate Systems Across Scales: From Colloidal Science to Geophysics, MA, USA, 2022.
- [42] J. F. Brady, G. Bossis, J. Fluid Mech. 1985, 155, 105.
- [43] G. K. Batchelor, J. Fluid Mech. 1970, 44, 419.
- [44] J. G. Kirkwood, P. L. Auer, J. Chem. Phys. 1951, 19, 281.
- [45] G. Bossis, A. Meunier, J. F. Brady, J. Chem. Phys. 1991, 94, 5064.
- [46] J. Čejková, M. Novák, F. Štěpánek, M. M. Hanczyc, Langmuir 2014, 30, 11937.
- [47] R. Fujita, T. Matsufuji, M. Matsuo, S. Nakata, Langmuir 2021, 37, 7039.
- [48] B. D. Frank, S. Djalali, A. W. Baryzewska, P. Giusto, P. H. Seeberger, L. Zeininger, Nat. Commun. 2022, 13, 2562.
- [49] G. Holló, N. J. Suematsu, E. Ginder, I. Lagzi, Sci. Rep. 2021, 11, 2753.
- [50] H. Xie, Z.-G. She, S. Wang, G. Sharma, J. W. Smith, Langmuir 2012, 28, 4459.
- [51] E. Acosta, Curr. Opin. Colloid Interface Sci. 2009, 14, 3.
- [52] B. X. Li, V. Borshch, R. L. Xiao, S. Paladugu, T. Turiv, S. V. Shiyanovskii, O. D. Lavrentovich, Nat. Commun. 2018, 9, 2912.
- [53] C. D. Ma, L. Adamiak, D. S. Miller, X. Wang, N. C. Gianneschi, N. L. Abbott, Small 2015, 11, 5747.
- [54] J. Wei, H. Yu, H. Liu, C. Du, Z. Zhou, Q. Huang, X. Yao, J. Mater. Sci. 2018, 53, 12056.
- [55] X.-L. Tang, S.-M. Guo, Z.-D. Liu, R.-Z. Tang, J.-Y. Pang, Y. Chen, in 2017 3rd Int. Forum Energy, Environ. Sci. Mater. (IFEESM 2017), Atlantis Press, Dordrecht, The Netherlands, 2018, pp. 598–602.
- [56] P. G. de Gennes, J. Prost, The Physics of Liquid Crystals, Clarendon Press, Oxford 1993.
- [57] J. Loudet, P. Barois, P. Poulin, Nature 2000, 407, 611.
- [58] P. S. Drzaic, Liquid Crystal Dispersions, World Scientific, Singapore 1995.
- [59] E. P. Raynes, R. J. A. Tough, K. A. Davies, Mol. Cryst. Liq. Cryst. 1979, 56, 63.
- [60] H. Hakemi, E. F. Jagodzinski, D. B. Dupré, Mol. Cryst. Liq. Cryst. 1983, 91, 129.
- [61] S. B. Chernyshuk, B. I. Lev, Phys Rev E 2011, 84, 011707.
- [62] K. Takahashi, M. Ichikawa, Y. Kimura, Phys. Rev. E 2008, 77, 020703.
- [63] J. Kotar, M. Vilfan, N. Osterman, D. Babič, M. Čopič, I. Poberaj, Phys. Rev. Lett. 2006, 96, 207801.
- [64] M. Vilfan, N. Osterman, M. Čopič, M. Ravnik, S. Žumer, J. Kotar, D. Babič, I. Poberaj, Phys. Rev. Lett. 2008, 101, 237801.
- [65] B. Mustin, B. Stoeber, Langmuir 2016, 32, 88.
- [66] Y.-Y. Luk, K.-L. Yang, K. Cadwell, N. L. Abbott, Surf. Sci. 2004, 570, 43.
- [67] M. A. Brown, Z. Abbas, A. Kleibert, R. G. Green, A. Goel, S. May, T. M. Squires, *Phys. Rev. X* 2016, 6, 011007.